

Supporting Information

Investigation of Programmable Friction with Ionic Liquid Mixtures at the Nano- and Macroscales

Felix Joachim Gatti ^{1,2,*,†}, **Wanhao Cai** ^{3,†}, **Richard Herzog** ³, **Amirmasoud Gharavian** ³, **Andreas Kailer** ¹, **Norman Baltes** ^{2,4}, **Peter Rabenecker** ^{2,4}, **Philipp Mörchel** ⁵, **Bizan N. Balzer** ^{3,6,7,*}, **Tobias Amann** ^{1,2} and **Jürgen Rühle** ^{6,8}

¹ Fraunhofer Institute for Mechanics of Materials IWM, MicroTribology Center μ TC, Woehlerstraße 11, 79108 Freiburg, Germany.

² Fraunhofer Cluster of Excellence Programmable Materials CPM, Wöhlerstraße 11, 79108, Freiburg, Germany.

³ Institute of Physical Chemistry, University of Freiburg, Albertstr. 21, 79104 Freiburg, Germany.

⁴ Fraunhofer Institute for Chemical Technology ICT, Joseph-von-Fraunhofer-Str. 7, 76327, Pfinztal, Germany.

⁵ Fraunhofer Institute for Integrated Circuits IIS, Am Hubland, 97074 Wuerzburg, Germany.

⁶ Cluster of Excellence livMatS @ FIT – Freiburg Center for Interactive Materials and Bioinspired Technologies, University of Freiburg, Georges-Köhler-Allee 105, 79104 Freiburg, Germany.

⁷ Freiburg Materials Research Center, University of Freiburg, Stefan-Meier-Str. 21, 79104 Freiburg, Germany.

⁸ IMTEK-Department of Microsystems Engineering, University Freiburg, Georges-Koehler-Allee 103, 79110, Freiburg, Germany.

[†] These authors contributed equally to this work.

^{*} Correspondence: felix.gatti@iwm.fraunhofer.de, bizan.balzer@physchem.uni-freiburg.de

Contents

Literature values on the influence of electrical potentials on the COF	3
Graphical abstract from Gatti et al. Towards programmable friction	4
Chemical structures of used ILs	5
Nanoscale and macroscale voltammetry-grams	6
AFM-based contact mechanics	7
Supporting data for FFM experiments	9
Static friction test A1 of the “multi-experiment”	11
3D-laser microscope wear analysis	12
AFM-based wear analysis	13
References	18

Literature values on the influence of electrical potentials on the COF

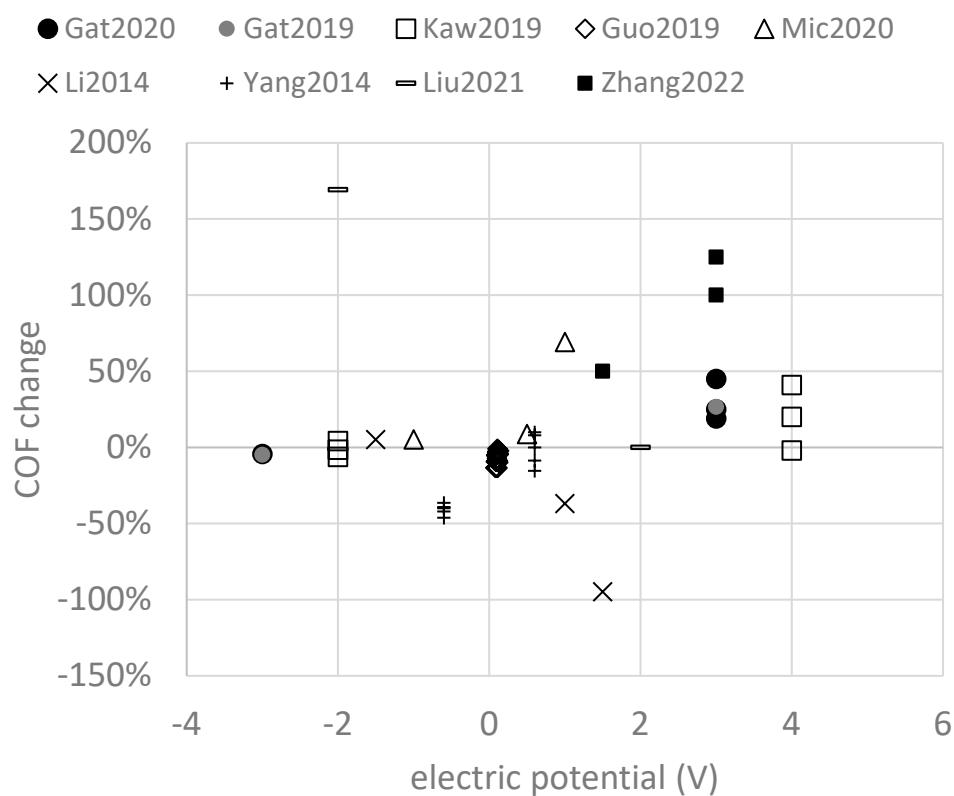


Figure S1. Literature values on the influence of the coefficient of friction (COF) by externally applied electrical potentials. [16,24,26,27,35,45-48]

Graphical abstract from Gatti et al.

Towards programmable friction.

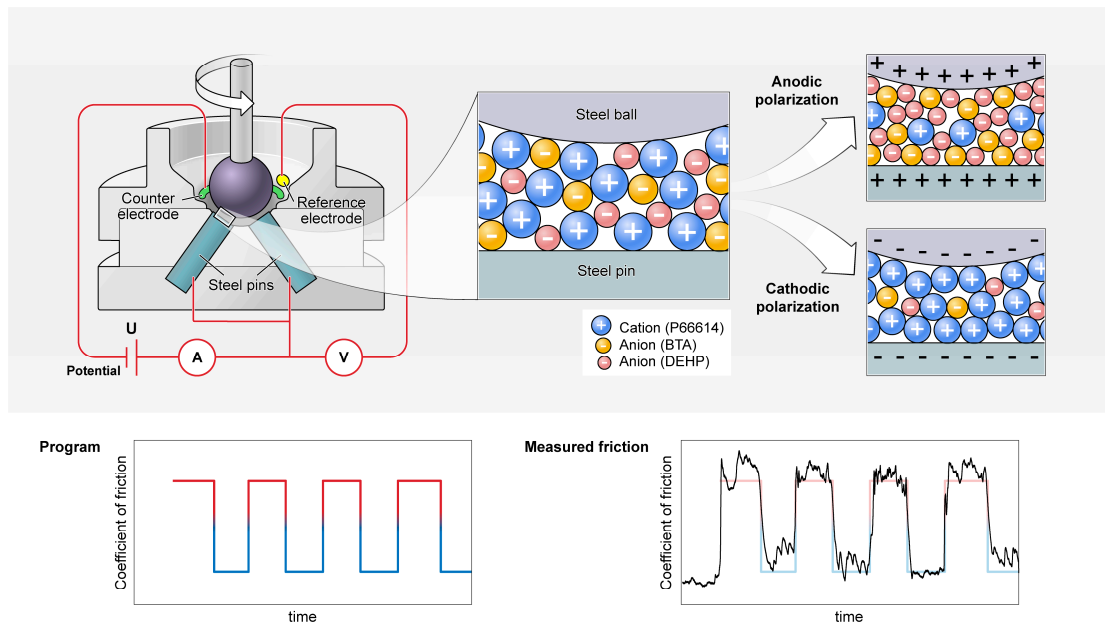


Figure S2. Graphical abstract from the 2020 publication by Gatti et al. to illustrate the different goals of the work. Here, the goal was to actively change, switch, and program friction during the tribological experiment by changing the potential at the working electrode. This could be achieved by adding and changing the concentration of the anions and cations, respectively [16].

Chemical structures of used ILs

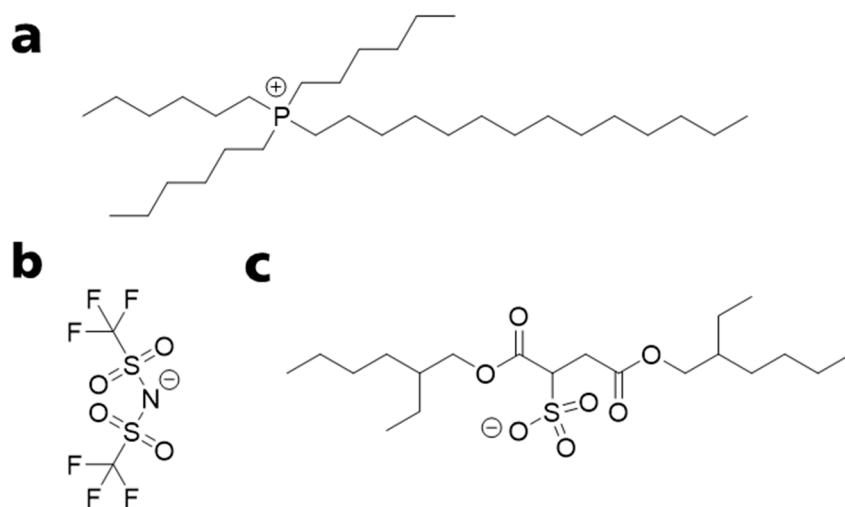


Figure S3. Chemical structures of the used ionic liquids. (a) Trihexyltetradecylphosphonium cation of the IL [P66614]. (b) Sulfonyl imide anion of the IL [P66614][BTA]. (c) Docusate anion of the IL [P66614][Doc].

Nanoscale and macroscale voltammograms

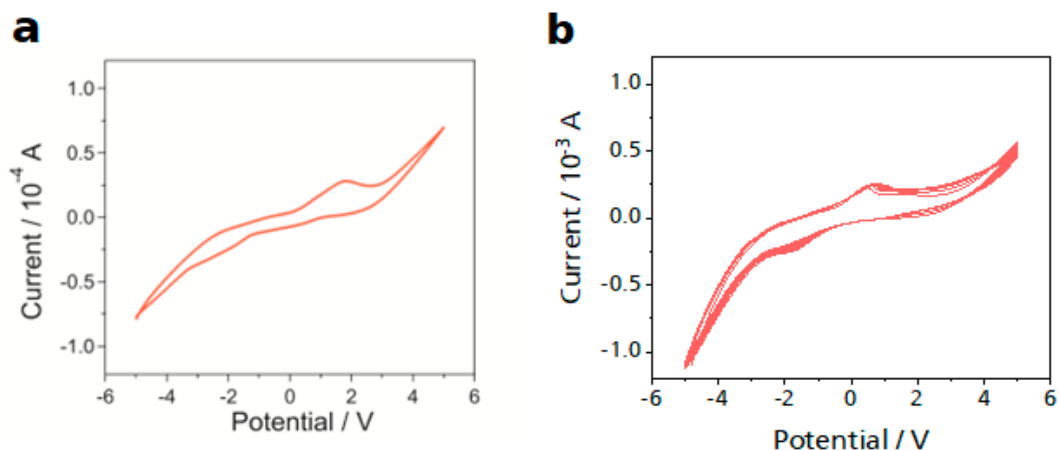


Figure S4. Comparison of nanoscale and macroscale voltammograms. (a) Voltammogram of the AFM-based EC cell, comprising an AFM cantilever carrying a borosilicate glass bead with a diameter size of 10 μm and a steel sample (connected to a Cu working electrode) immersed in ILM, a Pt counter electrode and an Ag reference electrode (three-electrode setup). Potentiostat parameters: scan rate: 0.1 V/s, sampling interval: 0.001 V, potential range: -5 V to +5 V. (b) Voltammogram of the ILM B4:D1 in the tribological setup in the tribometer. Three pins as working electrode, platinum wire as counter electrode and reference electrode (two-electrode-setup). Potentiostat parameters: scan rate: 0.1 V/s, potential range: -5 V to +5 V.

AFM-based contact mechanics

To determine the contact mechanics between the AFM tip attached glass sphere and the steel sample surface in the ILM (Figure S5a), we have measured the adhesion force between the two at different indentation forces. As shown in Figure S5b, the adhesion force is neglectable. Thus, we can use the Hertzian contact model to determine the contact pressure P and contact area A (Figure S5c) between a sphere and a flat surface by: [63]

$$P = \frac{1}{\pi} \left(\frac{6F_N E'}{r^2} \right)^{\frac{1}{3}} \quad (\text{Equation S1})$$

$$A = \pi \left(\frac{3F_N r}{4E'} \right)^{\frac{2}{3}} \quad (\text{Equation S2})$$

$$E' = \frac{1-\nu_1^2}{E_1} + \frac{1-\nu_2^2}{E_2} \quad (\text{Equation S3})$$

where r is the radius of the glass bead, E' is calculated via Eq. S3 with $E_1 = 72$ GPa and $E_2 = 193$ GPa the elastic moduli of glass and steel, respectively, [64,65] and $\nu_1 = \nu_2 = 0.3$ the Poisson's ratio of the glass and steel, respectively. [66] As shown in Figures S4c and d, the contact pressure ranges from 0.2 to 0.5 GPa, the contact area ranges from 10^3 to 10^4 nm².

As we have neglected the surface roughness of the contacting bodies, our calculation provides an estimate of a lower limit of the contact pressure P and an upper limit of the contact area A .

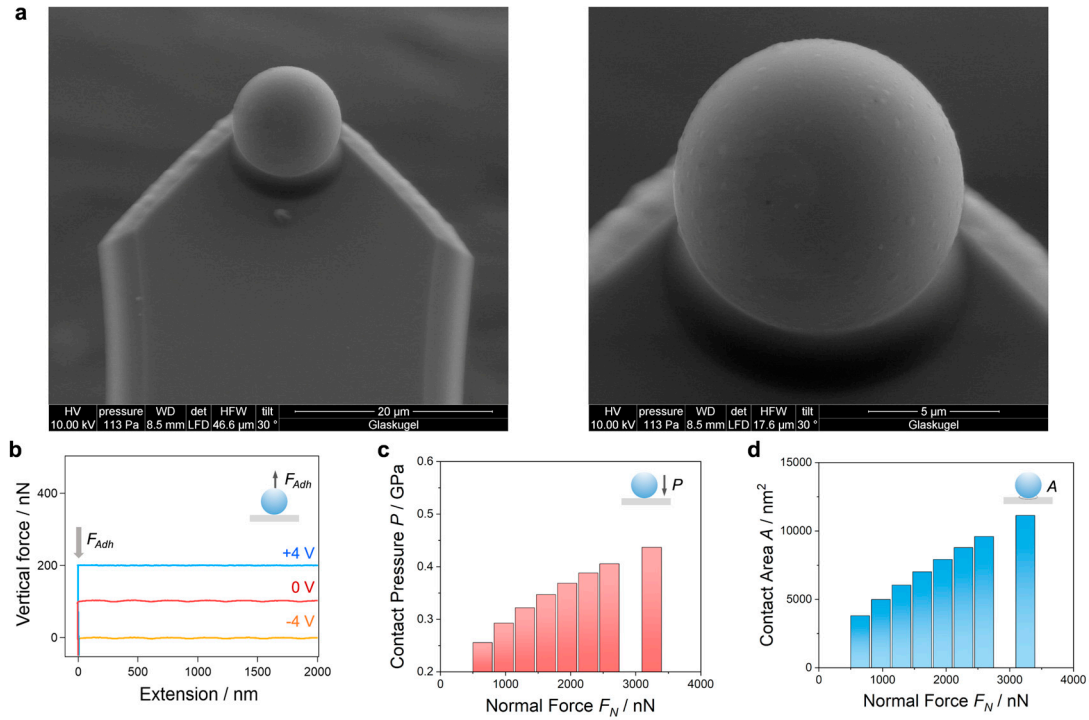


Figure S5. Contact mechanics between the glass bead and the steel surface in ILM. (a) SEM images of an exemplary AFM cantilever carrying a borosilicate glass bead with a diameter size of 10 μm (Novascan Technologies, USA). (b) Vertical force-extension curves (using vertical deflection, piezo driven distance, inverse optical lever sensitivity and force constant, taking the GetReal panel for automated calibration of the Cypher ES, see Materials and Methods, Section 2.2) between the glass bead and the steel surface are shown for different surface potentials for a normal force of $F_N = 3245$ nN (offset for 100 nN for a better presentation). The adhesion peak indicated by the gray arrow is the adhesive force F_{Adh} between the glass bead and the steel surface, which was negligible compared to the applied trigger forces. (c) The contact pressure P and (d) the contact area A between the glass bead and the steel surface determined by the Hertz model is given for each of the applied normal forces F_N .

Supporting data for FFM experiments

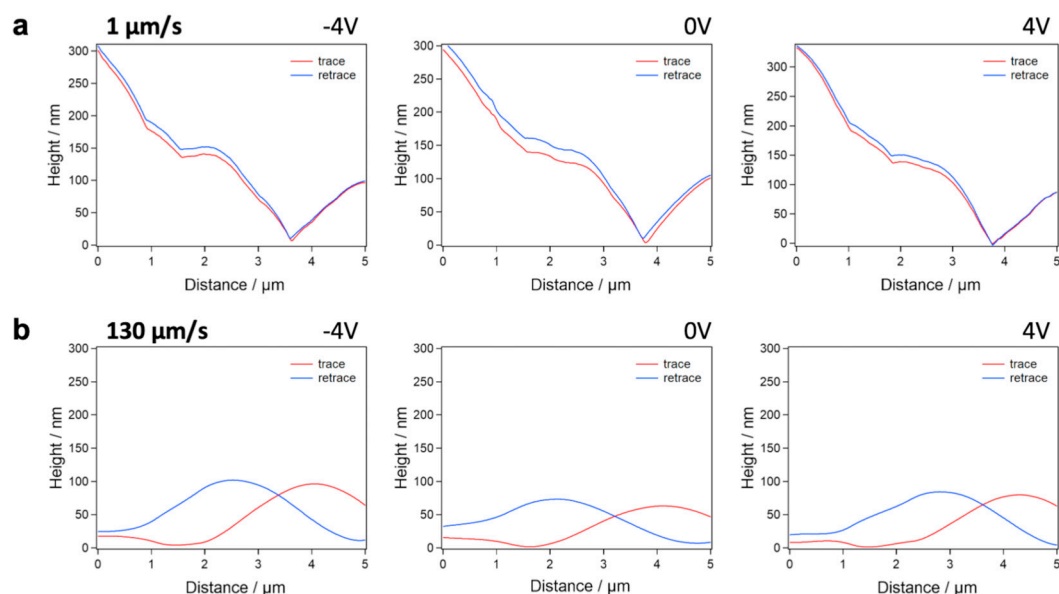


Figure S6: Height profile of the FFM experiment. Exemplary height profiles for trace and retrace obtained at $F_N = 649$ nN are shown for (a) a velocity $v = 1$ $\mu\text{m/s}$ and (b) $v = 130$ $\mu\text{m/s}$. From left to right: surface potentials applied to the steel surface -4, 0 and +4 V. All of the height profiles were taken on the same scanning line. Note that the 10 μm bead is far from being a sharp cantilever tip such as used for imaging, where the topography is locally well resolved.

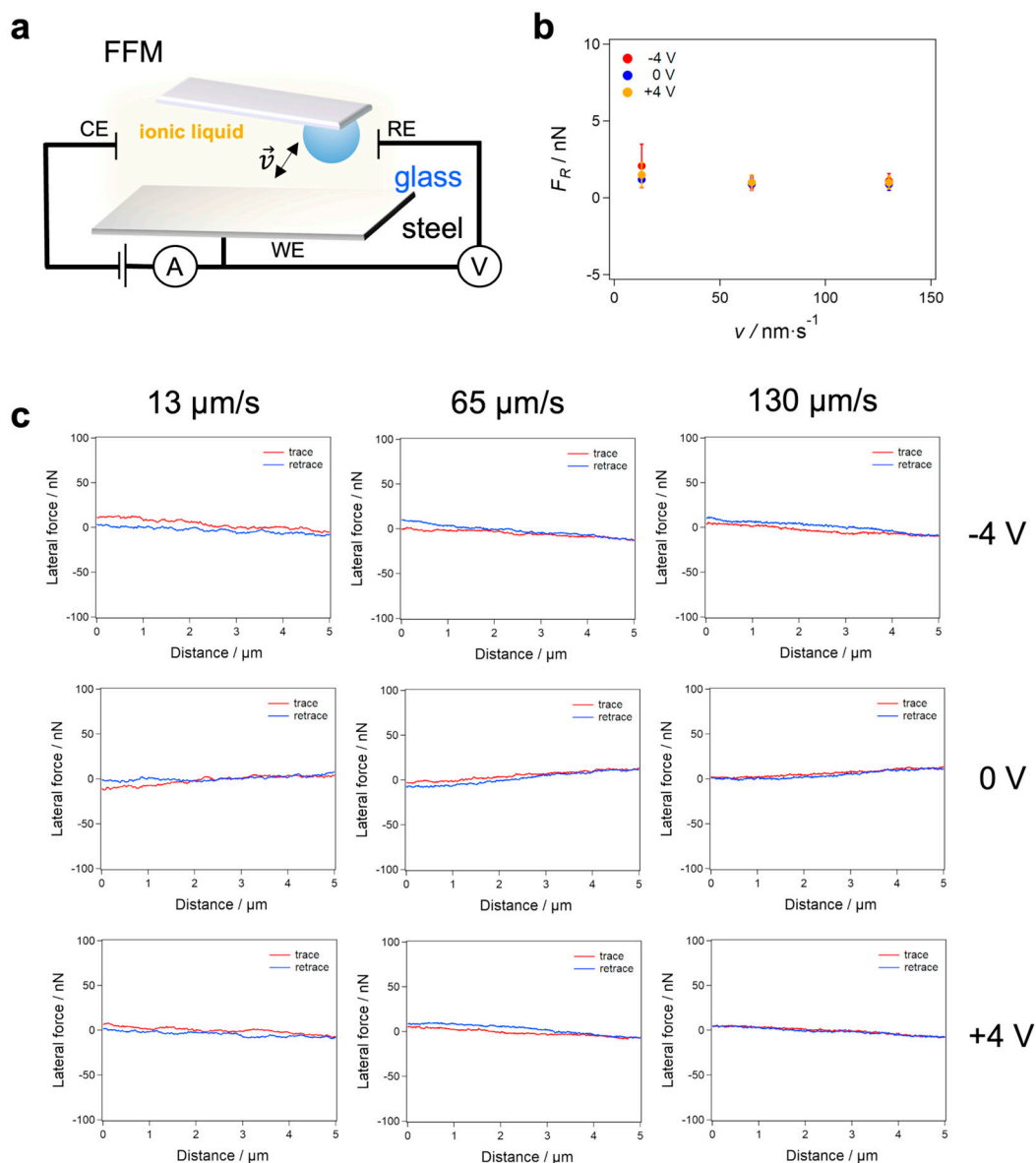


Figure S7: Impact of ILM on FFM experiments. (a) Scheme of the experiment: a glass bead is moved through the ILM without contacting any surface underneath. To do so the glass bead is retracted far away from the surface (for 1000 μm) to avoid any effect from the surface. (b) Friction forces F_R under different velocities (1-130 $\mu\text{m/s}$) were all in the range of 1 nN, indicating that the viscous friction between the cantilever attached glass bead and the ILM is neglectable compared to the friction forces obtained in contact with the steel sample. (c) Exemplary friction loops at different velocities corresponding to the friction forces F_R shown in (b). The friction loops between trace and retrace show that the contribution of solvent related friction was orders of magnitude lower than those between glass bead and steel surface (Figure 3).

Static friction test A1 of the “multi-experiment” and current flow

static friction (A1)

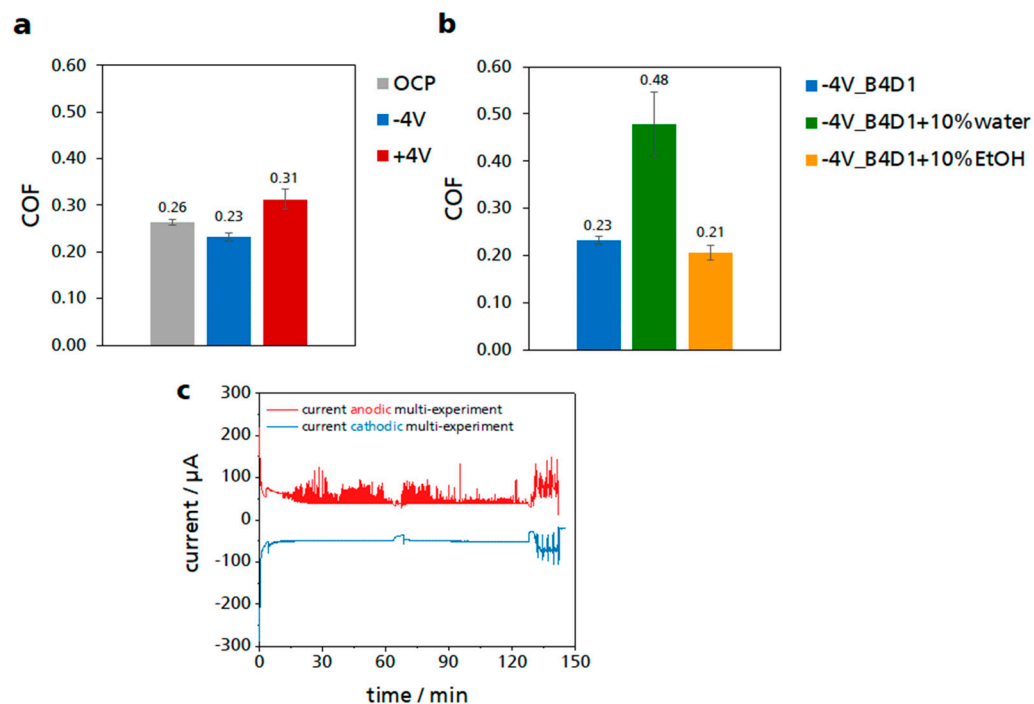


Figure S8. Multi-experiment of the section A1 with (a) the pure ILM B4:D1 and (b) the ILM with the addition of water and ethanol, respectively. (c) Course of the current flow during the entire multi-experiment at anodic (red line) and cathodic (blue line) potential.

3D-laser microscope wear analysis

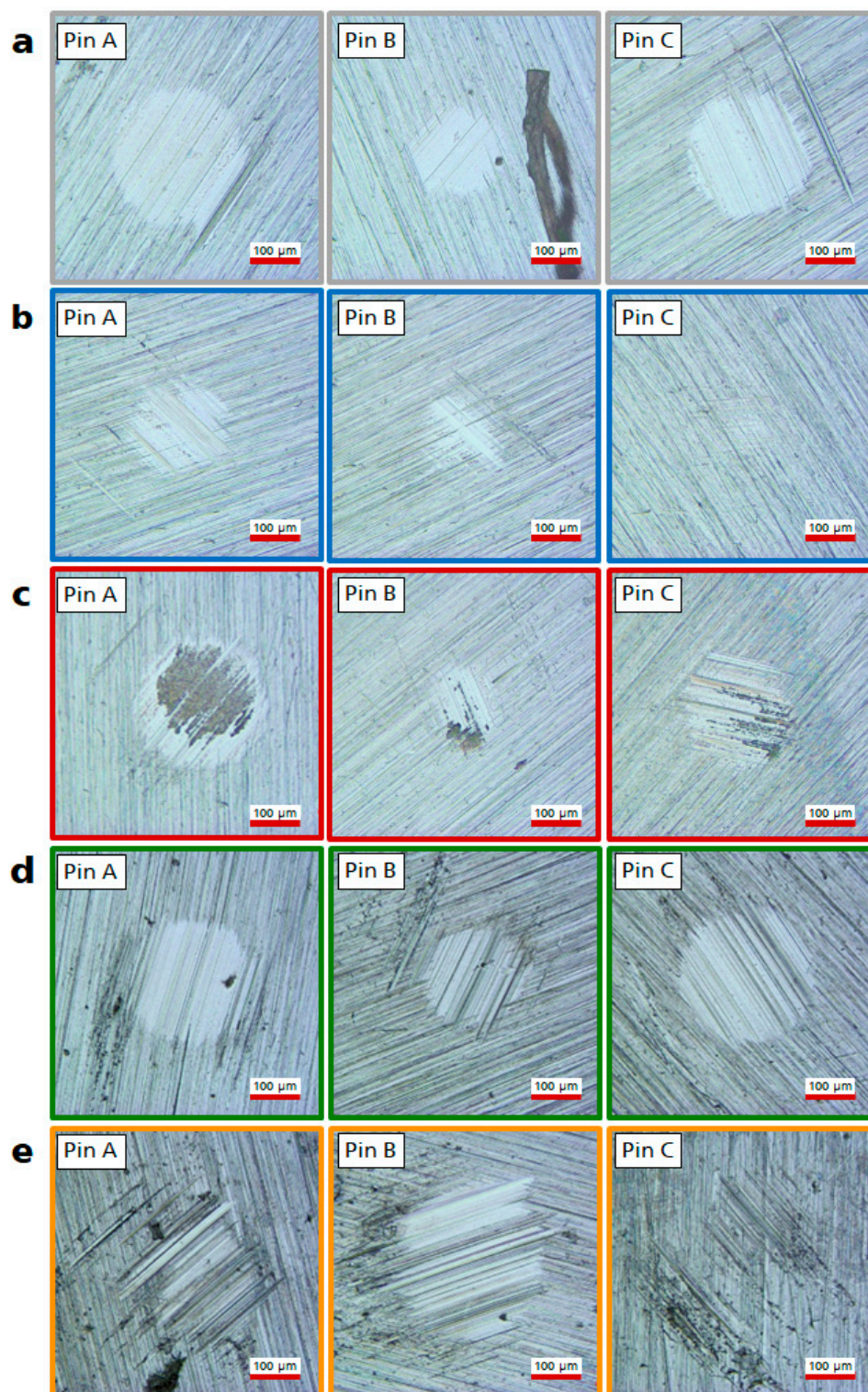


Figure S9. Wear traces after the multi-experiment taken with the Keyence VK-9710 3D laser microscope ordered by the respective voltage (vs. platinum) and lubricant. (a) At OCP with ILM B4:D1, (b) at -4 V with ILM B4:D1, (c) at +4 V with ILM B4:D1, (d) at -4 V with ILM B4:D1+10 % water and (e) at -4 V with ILM B4:D1+10 % ethanol.

AFM-based wear analysis

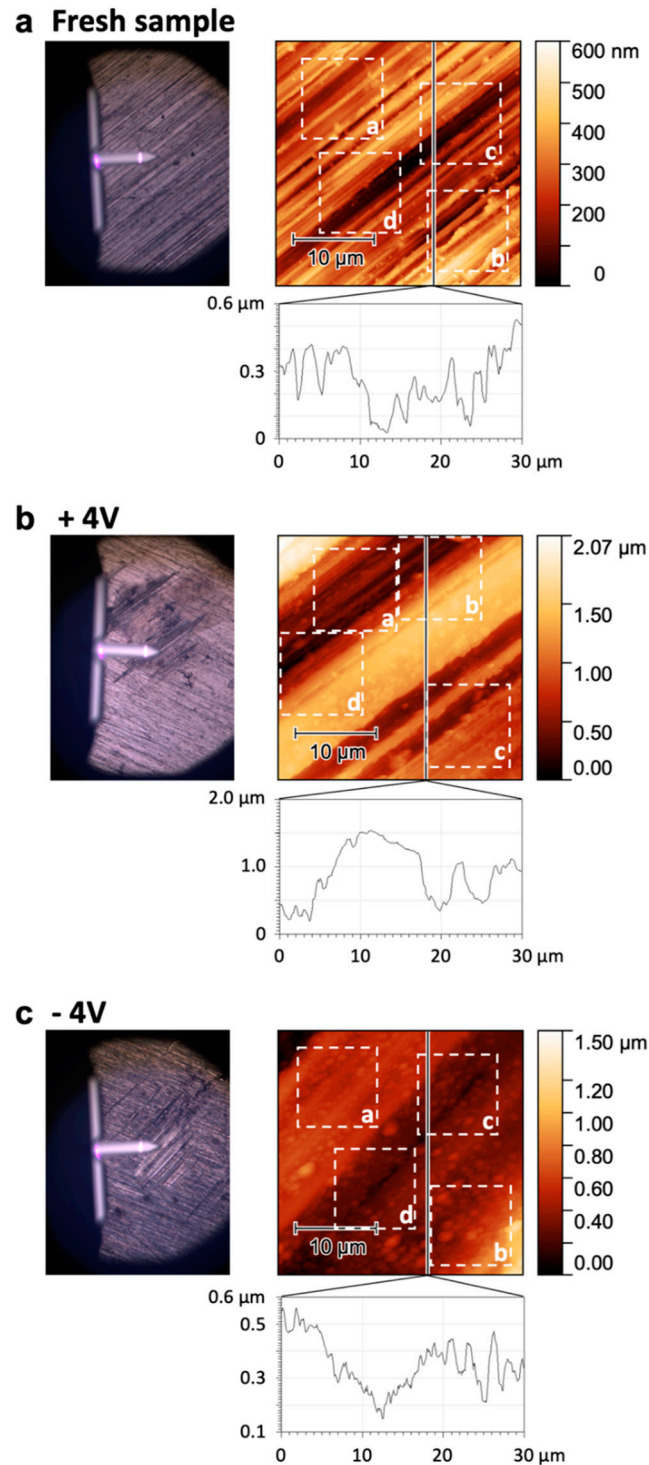


Figure S10. Microscopic wear of steel pins. AFM images ($30 \times 30 \mu\text{m}^2$, scan area $900 \mu\text{m}^2$) for (a) fresh steel pins and (b and c) steel pins after tribometer experiments ($\pm 4 \text{ V}$) with ILM. Optical images show the region of AFM image acquisition, $10 \times 10 \mu\text{m}^2$ regions (dashed boxes indicating different regions a-d, scan area $100 \mu\text{m}^2$) are used for a detailed RMS roughness determination and line profiles are given for the indicated lines.

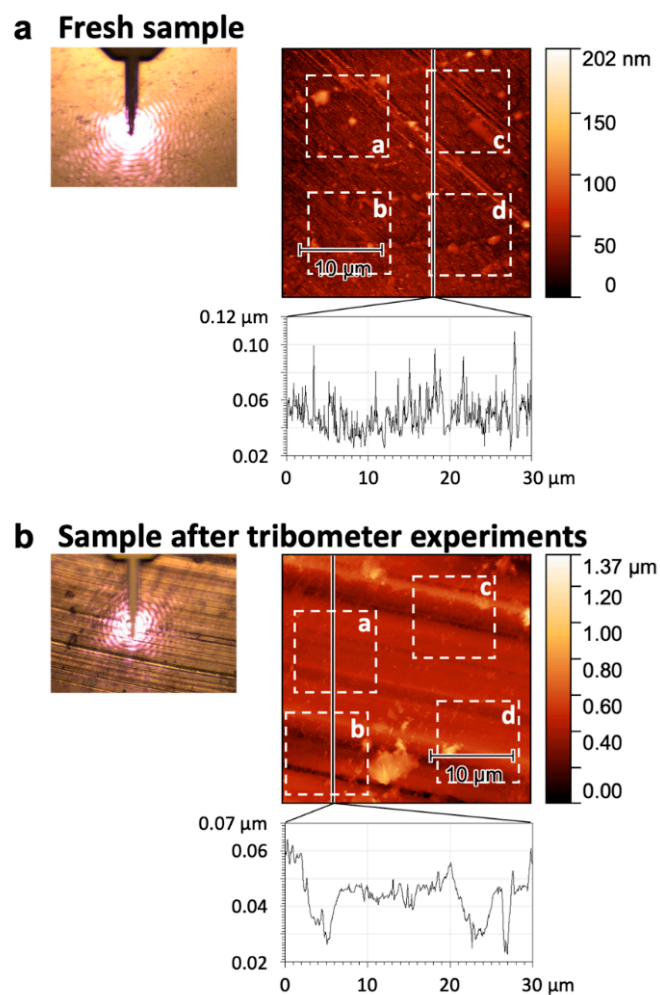


Figure S11: Microscopic wear of steel balls. AFM images ($30 \times 30 \mu\text{m}^2$, scan area $900 \mu\text{m}^2$) for (a) fresh steel balls and (b) steel balls after tribometer experiments with ILM. Optical images show the region of AFM image acquisition, $10 \times 10 \mu\text{m}^2$ regions (dashed boxes indicating different regions a-d, scan area $100 \mu\text{m}^2$) are used for a detailed RMS roughness determination and line profiles are given for the indicated lines.

Solid state NMR-analysis

Nuclear Magnetic Resonance (NMR) relaxation data were measured using the Polymer-Profiler, a 0.5 Tesla (approx. 22.8 MHz proton Larmor frequency) benchtop NMR system from Pure Devices (Germany) and Fraunhofer IIS (Würzburg, Germany). The processing of the NMR data was performed with Matlab (MathWorks, USA). All lubricants were measured at a constant magnet and sample temperature of 30 °C. The samples were filled in an 8 mm inner diameter glass tube which was filled to a height of approx. 8 mm (the tube of the sample after the multi-experiment with OCP was only filled to approx. 4 mm height since we had not enough sample material). Here, only the proton (¹H) NMR signal was detected and used for further processing of the relaxation measurements.

The T₁ relaxation measurement was realized using a saturation recovery experiment. One FID per repetition was recorded at different timepoints after the saturation pulses. Overall, 16 FIDs were recorded at 16 timepoints ranging from 30 ms to 3 s after the last saturation pulse. The duration of the saturation delay was increased exponentially (i.e., the first points of the saturation recovery curve were sampled at a denser time raster than the later ones). The T₁ measurement parameters were the following: 16 averages, 16 FIDs after saturation, 5 MHz as sampling frequency, 2048 of sample points of single FID, 9 saturation pulses, 5 µs between sat. pulses, 30 ms / 3000 ms (exponentially) as min. / max. saturation recovery time, 3.5 s repetition time and a blockpulse of 4.4 µs as sat. / excitation pulse (90°). The T₁ relaxation curve was modeled and fitted by a bi-exponential function:

$$f_{T_1}(t) = M_{0,a} \cdot \left(1 - M_{0,imp} \cdot e^{-t/T_{1,a}}\right) + M_{0,b} \cdot \left(1 - M_{0,imp} \cdot e^{-t/T_{1,b}}\right) \quad (\text{Equation S4})$$

Where $M_{0,imp}$ should be 1 for a perfect saturation (i.e., imperfections in the saturation are addressed by this parameter). $M_{0,a}$ ($M_{0,b}$) describes the relative contribution of the relaxation time $T_{1,a}$ ($T_{1,b}$) to the relaxation curve.

The T₂ measurements were performed using a Carr–Purcell–Meiboom–Gill (CPMG) multi spin echo measurement sequence. The T₂ measurement parameters were the following: 128 averages, 6500 echos, 5 MHz as sampling frequency, 16 sample points of single echo, 100 µs as inter echo time, 3 s as repetition time and a blockpulse of 4.4 µs as refocusing (180°) / excitation pulse (90°). The T₂ relaxation curve was modeled and fitted by a bi-exponential function:

$$f_{T_2}(t) = M_{0,a} \cdot e^{-t/T_{2,a}} + M_{0,b} \cdot e^{-t/T_{2,b}} \quad (\text{Equation S5})$$

$$f_{T_1}(t) = M_0 \cdot (1 - (1 + t \cdot \theta)^{-\kappa}) \quad (\text{Equation S6})$$

$$f_{T_2}(t) = M_0 \cdot (1 + t \cdot \theta)^{-\kappa} \quad (\text{Equation S7})$$

The mean relaxation times T₁ and T₂ could be calculated by:

$$T_{1,2} = 1/(\kappa \cdot \theta) \quad (\text{Equation 14})$$

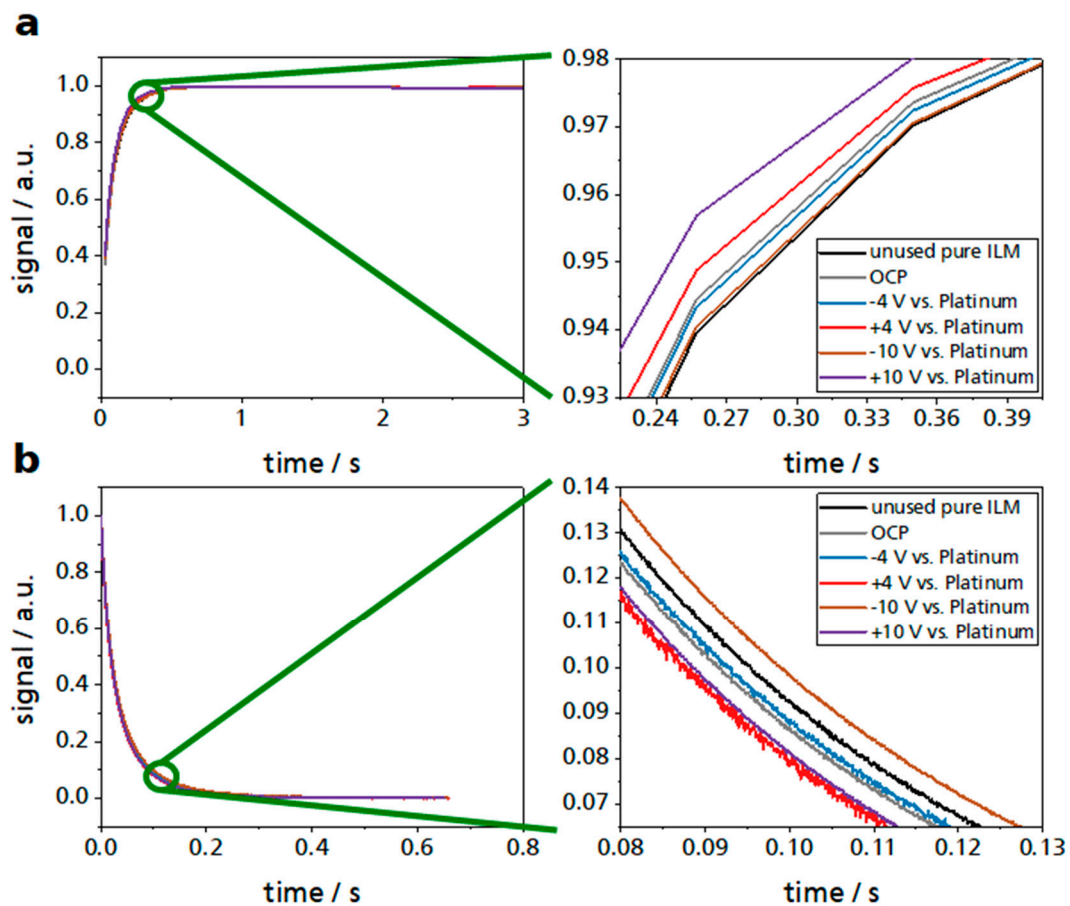


Figure S12: Influence of chemical reaction by solid state NMR analysis. (a) T_1 and (b) T_2 relaxation times of the used and pristine ILM. NMR was used to test both the ILMs investigated in the multi-experiment and ILMs exposed to a voltage outside the stable range of the ILM.

Table S1. Roughness analysis of wear regions of the steel pins. RMS roughness from AFM images, with scan sizes of 30·30 μm^2 (scan area 900 μm^2) and 10·10 μm^2 regions a-d according to AFM images shown in Figure S10 (area 100 μm^2) for fresh steel pins and steel pins after tribometer experiments (± 4 V) with ILM.

sample	RMS roughness / nm				
	full image	a	b	c	d
Fresh	99	73	111	105	96
After tribometer test +4 V	410	272	455	186	422
After tribometer test -4 V	170	45	207	73	83

Table S2. Roughness analysis of wear regions of the steel balls. RMS roughness using AFM images, with scan sizes of 30·30 μm^2 (scan area 900 μm^2) and 10·10 μm^2 regions a-d according to AFM images shown in Figure S11 (scan area 100 μm^2) for a fresh steel ball and a steel ball after tribometer experiments with ILM.

sample	RMS roughness / nm				
	full image	a	b	c	d
Fresh	11	17	12	13	13
After tribometer test	97	28	95	84	96

References

16. Gatti, F.; Amann, T.; Kailer, A.; Baltes, N.; R  he, J.; Gumbsch, P. Towards programmable friction: control of lubrication with ionic liquid mixtures by automated electrical regulation. *Sci Rep* **2020**, *10*, 17634, doi:10.1038/s41598-020-74709-2.
24. Zhang, C.; Chen, J.; Liu, M.; Wang, F.; Zheng, Y.; Cheng, Y.; Liu, Z. Relationship between Viscosity and Resistance of Oil Film: A New Way to Investigate the Controllable Friction between Charged Interfaces Lubricated by Ionic Lubricating Oil. *Adv. Mater. Interfaces* **2022**, 2200229, doi:10.1002/admi.202200229.
26. Li, H.; Wood, R.J.; Rutland, M.W.; Atkin, R. An ionic liquid lubricant enables superlubricity to be "switched on" in situ using an electrical potential. *Chemical Communications* **2014**, *50*, 4368–4370, doi:10.1039/c4cc00979g.
27. Liu, C.; Fang, J.; Wen, X.; Tian, Y.; Meng, Y. Active Control of Boundary Lubrication of Ceramic Tribo-Pairs in Sodium Dodecyl Sulfate Aqueous Solutions. *Tribol Lett* **2021**, *69*, 1–14, doi:10.1007/s11249-021-01518-7.
35. Felix Gatti; Tobias Amann; Andreas Kailer; Johannes Abicht; Peter Rabenecker; Norman Baltes; J  rgen R  he. Makroskopische Reibwertsteuerung durch elektrochemische Potentiale mit ionischen Fl  ssigkeiten. *Tribologie und Schmierungstechnik* **2019**, *66*, doi:10.30419/TuS-2019-0024.
45. Kawada, S.; Ogawa, S.; Sasaki, S.; Miyatake, M. Friction Control by Applying Electric Potential under Lubrication with Ionic Liquids. *Tribology Online* **2019**, *14*, 71–77, doi:10.2474/trol.14.71.
46. Guo, Y.; Liu, G.; Li, G.; Zhao, F.; Zhang, L.; Guo, F.; Zhang, G. Solvent-free ionic silica nanofluids: Smart lubrication materials exhibiting remarkable responsiveness to weak electrical stimuli. *Chemical Engineering Journal* **2020**, *383*, 123202, doi:10.1016/j.cej.2019.123202.
47. Michalec, M.; Svoboda, P.; Krupka, I.; Hartl, M.; Venc  l, A. Investigation of the tribological performance of ionic liquids in non-conformal EHL contacts under electric field activation. *Friction* **2020**, *8*, 982–994, doi:10.1007/s40544-019-0342-y.
48. Yang, X.; Meng, Y.; Tian, Y. Effect of Imidazolium Ionic Liquid Additives on Lubrication Performance of Propylene Carbonate under Different Electrical Potentials. *Tribol Lett* **2014**, *56*, 161–169, doi:10.1007/s11249-014-0394-0.
63. Guo, D.; Li, J.; Xie, G.; Wang, Y.; Luo, J. Elastic properties of polystyrene nanospheres evaluated with atomic force microscopy: size effect and error analysis. *Langmuir* **2014**, *30*, 7206–7212, doi:10.1021/la501485e.
64. Montagne, A.; Tromas, C.; Audurier, V.; Woirgard, J. A new insight on reversible deformation and incipient plasticity during nanoindentation test in MgO. *J. Mater. Res.* **2009**, *24*, 883–889, doi:10.1557/jmr.2009.0127.
65. Mente, P.L.; Lewis, J.L. Elastic modulus of calcified cartilage is an order of magnitude less than that of subchondral bone. *J. Orthop. Res.* **1994**, *12*, 637–647, doi:10.1002/jor.1100120506.
66. Bertoldi, K.; Reis, P.M.; Willshaw, S.; Mullin, T. Negative Poisson's ratio behavior induced by an elastic instability. *Advanced Materials* **2010**, *22*, 361–366,

doi:10.1002/adma.200901956.